ACS Photonics

pubs.acs.org/journal/apchd5

Article

Accessing the Exceptional Points in a Graphene Plasmon–Vibrational Mode Coupled System

Sang Hyun Park,* Shengxuan Xia,* Sang-Hyun Oh,* Phaedon Avouris,* and Tony Low*

Cite This: https://doi.org/10.1021/acsphotonics.1c01083

Read Online

ACCESS | Metrics & More | Article Recommendations | Supporting Information

ABSTRACT: The coupling of plasmons and vibrational modes has been routinely observed in graphene and other 2D systems in both near-field and far-field spectroscopy. However, the relation between coupling strength and modal losses, and exceptional point physics has not been discussed. Here we apply a non-Hermitian framework to a model system of molecular layers on graphene and show that the transition point between strong and weak coupling regimes coincides with the exceptional point of non-Hermitian physics. We further show that the exceptional point can be conveniently located by changing the incident angle of the light and the graphene Fermi energy. Finally, we show that enhanced spectral sensitivity is obtained from small changes in molecular film thickness when the system is tuned to the exceptional point.

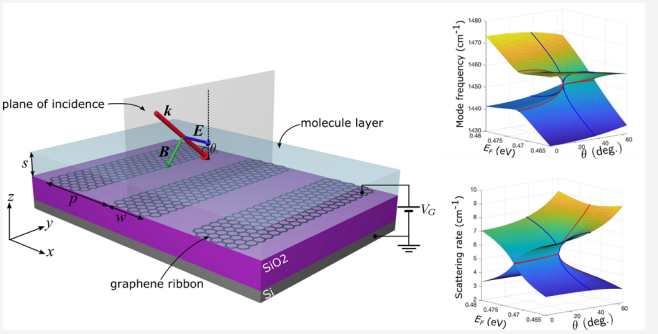

KEYWORDS: *exceptional point, graphene, plasmon, coupled-mode model, PT-symmetry*

The response of coupled systems has been shown to strongly depend on the relative strength of their coupling and losses. Here we will be focusing on the coupling between a graphene plasmon and a vibrational mode. At resonance, when the coupling is strong relative to the losses, the mode degeneracy is lifted, giving rise to hybridized modes at split frequencies.[1] The resulting absorption spectrum has two peaks that are separated by $\Delta\omega \gg \gamma$, where γ is the line width. When the coupling is weak, the peak's degeneracy is no longer lifted, but these degenerate modes can still interfere. In the limit of contrasting line widths ($\gamma_1 \gg \gamma_2$), destructive interference between the modes results in a sharp optical transparency region within a broad absorption peak.[2] Such "strong" and "weak" coupling response has been observed in many physical systems, including three-level atoms,[3] whispering-gallery-mode micro-resonators,[4] mechanical systems,[5] and plasmonics.[6,7]

The role of coupling (κ) and loss (γ) is also an important factor in non-Hermitian sytems,[8] which are open systems that exchange energy with their environment. The importance of coupling and loss is highlighted in a subset of non-Hermitian systems that obey parity-time (PT) symmetry.[9] When $\kappa/\gamma > 1$, the eigenstates of the system are PT symmetric and the eigenvalues are real. When $\kappa/\gamma < 1$, the eigenstates are no longer PT symmetric, and the eigenvalues become complex. At $\kappa = \gamma$, there is a non-Hermitian singularity, also known as the exceptional point (EP), where both the eigenvalues and eigenvectors coalesce. This transition has been utilized to demonstrate nonreciprocal propagation in waveguides,[10] asymmetric transmission of polarized light,[11] and PT-symmetric lasers.[12] Also, systems at exceptional points have been reported to exhibit enhanced sensitivity to perturbations.[13−15]

Plasmons in graphene couple with vibrational modes, and this interaction has been experimentally observed in various contexts. For example, when patterned graphene is placed on a silicon dioxide substrate, coupling with the substrate surface optical phonon modes are directly observable in the extinction spectra.[16] Coupling with surface modes in atomically thin polar materials such as hBN was also observed.[17] For bilayer graphene, plasmons couple with its intrinsic Γ point optical phonon, resulting in a sharp phonon-induced transparency.[18,19] Finally, the high confinement of graphene plasmons also allows them to couple with vibrational modes of adsorbed molecular layers or gases, enabling spectral fingerprinting through their extinction spectra.[20−25]

In this paper, we discuss the coupling of graphene plasmons with vibrational modes from the perspective of a non-Hermitian system, highlighting the interplay between coupling and loss. By applying a mode decomposition process called harmonic inversion analysis,[26] we systematically find the mode frequencies and losses of the coupled modes from the absorption spectra of the system. Using the graphene Fermi energy and incidence

Received: July 17, 2021

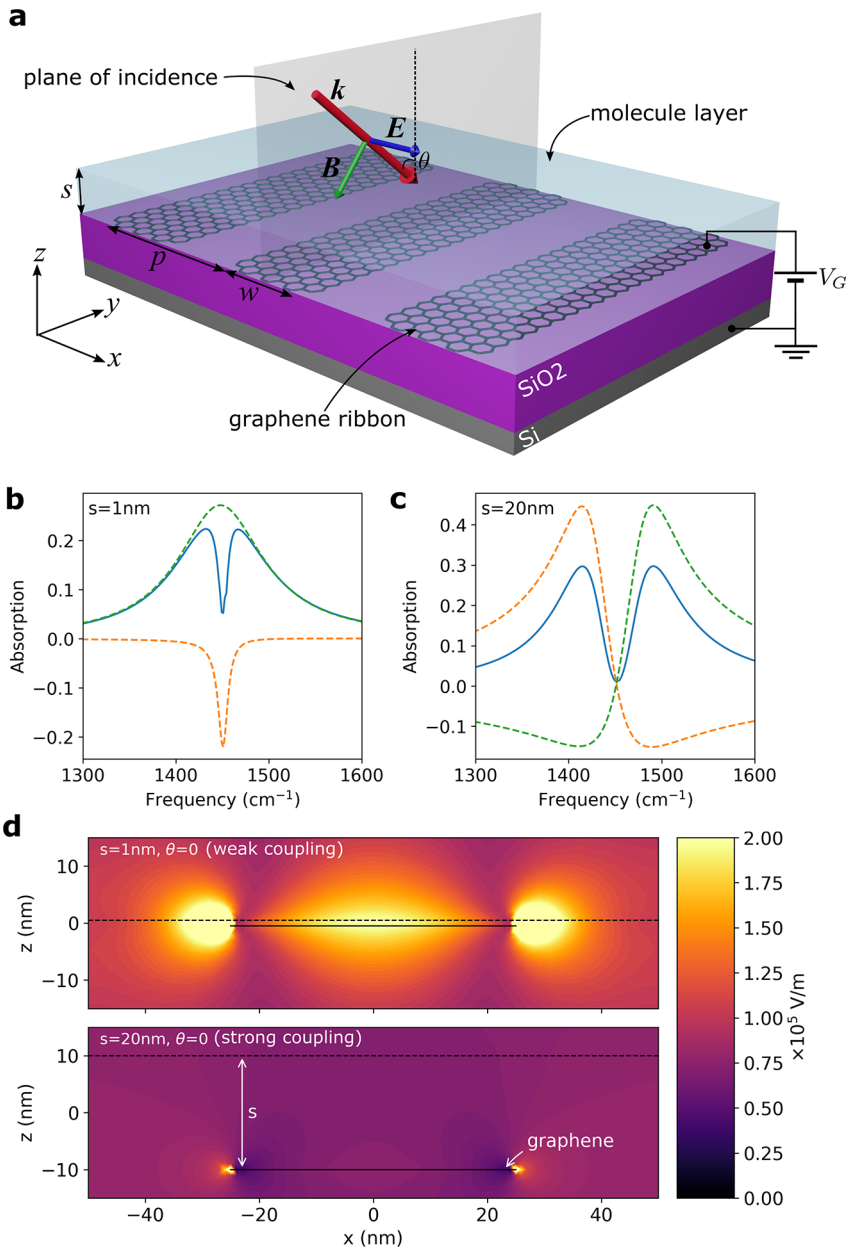

Figure 1. (a) Schematic of the structure. By patterning graphene into ribbons of width w = 50 nm and periodicity p = 100 nm we excite plasmons with $q = \pi/w$[30] under incident light polarized along the width of the nanoribbons. Absorption spectra for (b) weak coupling (s = 1 nm) and (c) strong coupling (s = 20 nm), where s is the thickness of the molecular layer. The dashed lines show results of decomposition using the harmonic inversion analysis method. (d) $|E_x|$ fields for weak (s = 1 nm) and strong (s = 20 nm) coupling are shown for ω = 1450 cm^{-1}.

angle of light as tunable parameters, we map out the eigenvalue surface of the coupled system and show the existence of an exceptional point (EP). Furthermore, at fixed Fermi energy, we show that the system undergoes a PT-breaking transition at the EP, which may also be identified as a transition from weak to strong coupling. Non-Hermitian and exceptional point physics provides a unique perspective in the understanding of coupled systems, and the approach we outline here sets the stage for the future design of sensing plasmon−vibrational mode coupling characteristics via the EP.

EXCEPTIONAL POINT PHYSICS FROM A COUPLED MODE MODEL

Exceptional point physics in coupled systems can be elucidated from using a simple coupled mode formulation.[27] Consider graphene covered by a material with a vibrational mode ω_0. The equations of motion for the plasmon ($a(t)$) and vibrational mode ($b(t)$) amplitudes are

$$\dot{a}(t) = i\omega_{pl}a - \gamma_{pl}a + i\kappa b + \sqrt{\gamma_{pl,e}}s_{a,in} \quad (1)$$

$$\dot{b}(t) = i\omega_0 b - \gamma_0 b + i\kappa a \quad (2)$$

where $\gamma_{pl} = \gamma_{pl,e} + \gamma_{pl,i}$ accounts for plasmon loss, including contributions from electron scattering channels in graphene (intrinsic contribution, $\gamma_{pl,i}$) and coupling of the plasmon resonance with free space radiation (extrinsic contribution, $\gamma_{pl,e}$), γ_0 is the vibrational mode loss, ω_{pl} and ω_0 are the resonant frequencies of the plasmon and vibrational mode, κ is the near-field coupling strength, and $s_{a,in}$ quantifies the input field that

https://doi.org/10.1021/acsphotonics.1c01083
ACS Photonics XXXX, XXX, XXX−XXX

couples into the plasmon. Assuming that the amplitudes have a $e^{i\omega t}$ time dependence, the response of the plasmon is given by

$$a(t) = \frac{i\sqrt{\gamma_{\mathrm{pl,e}}}s_{\mathrm{a,in}}(\omega - \tilde{\omega}_0)}{\kappa^2 - (\omega - \tilde{\omega}_{\mathrm{pl}})(\omega - \tilde{\omega}_0)}e^{i\omega t} \tag{3}$$

where we have defined $\tilde{\omega}_{\mathrm{pl}/0} = \omega_{\mathrm{pl}/0} + i\gamma_{\mathrm{pl}/0}$. From eq 3, a resonant response occurs when $\omega_{\pm} = (\tilde{\omega}_{\mathrm{pl}} + \tilde{\omega}_0)/2 \pm \sqrt{(\tilde{\omega}_{\mathrm{pl}} - \tilde{\omega}_0)^2 + 4\kappa^2}/2$. When $\omega_{\mathrm{pl}} = \omega_0$, the poles are at $\omega_{\pm} = \omega_0 + i\overline{\gamma} \pm \sqrt{\kappa^2 - \gamma^2}$, where we have defined $\overline{\gamma} = (\gamma_{\mathrm{pl}} + \gamma_0)/2$ and $\gamma = (\gamma_{\mathrm{pl}} - \gamma_0)/2$. Written in this form, we see that there is a transition at the poles for $\kappa = \gamma$. The poles found from eq 3 can be identified with the eigenvalues of a matrix[28] of the form

$$\hat{H} = \begin{pmatrix} \omega_{\mathrm{pl}} + i\gamma_{\mathrm{pl}} & \kappa \\ \kappa & \omega_0 + i\gamma_0 \end{pmatrix} \tag{4}$$

which is a general non-Hermitian matrix. For the condition $\omega_{\mathrm{pl}} = \omega_0$ the matrix above describes a passive PT symmetric system,[29] which exhibits the same behavior with PT symmetric systems that have balanced loss and gain. By making this connection, we see that the transition point at $\kappa = \gamma$ may be identified as the exceptional point of non-Hermitian Hamiltonians. If we consider a system in which the coupling is fixed and loss is tunable, writing $\gamma = \kappa + \Delta\gamma$ gives the eigenvalues

$$\omega_{\pm} = \omega_0 + i\overline{\gamma} \pm i\sqrt{\Delta\gamma}\sqrt{\Delta\gamma + 2\kappa} \tag{5}$$

This shows the characteristic square-root dependence of the mode splitting under perturbations near an EP.[13]

MODE SPLITTING AT THE EXCEPTIONAL POINT

The coupling of plasmons in graphene with vibrational modes can be studied through a far-field scattering experiment via its absorption spectrum. Here, we numerically calculate the scattering coefficients[31] for a typical device consisting of an array of electrostatically gated graphene nanoribbons as illustrated in Figure 1a. Graphene was modeled as a surface current density with conductivity given by

$$\sigma_{\mathrm{gr}}(\omega) = \frac{\sigma_0}{\pi}\frac{4E_{\mathrm{F}}}{\hbar\gamma_{\mathrm{gr}} - i\hbar\omega} \tag{6}$$

where $\sigma_0 = e^2/4\hbar$. The lifetime of carriers in graphene is set to $\tau_{\mathrm{gr}} = \gamma_{\mathrm{gr}}^{-1} = 50$ fs, which has been shown to be dominated by edge scattering.[16] Other contributions include electron−electron scattering[32] and electron-impurity scattering.[33,34] The periodic ribbon structure is accounted for by writing the conductivity as a Fourier series

$$\sigma_{\mathrm{GNR}}(\omega, x) = \sum_m \tilde{\sigma}_m(\omega)e^{imGx} \tag{7}$$

$$\tilde{\sigma}_m(\omega) = \frac{\sigma_{\mathrm{gr}}(\omega)}{p}\int_0^p \Theta(x - w)e^{-imGx}\,\mathrm{d}x \tag{8}$$

where p is the periodicity, w is the ribbon width, $G = 2\pi/p$ is the reciprocal lattice vector, and $\Theta(x)$ is the Heaviside step function. The vibrational mode is modeled using the dipole oscillator model

$$\epsilon(\omega) = \epsilon_\infty + \frac{f\omega_0^2}{\omega_0^2 - \omega^2 - i\gamma_0\omega} \tag{9}$$

where ω_0 is the vibrational mode frequency, γ_0 is the scattering rate, ϵ_∞ is the high frequency limit of the dielectric function, and f is the oscillator strength. For concreteness, we set $\omega_0 = 1450$ cm^{-1}, $\tau_0 = \gamma_0^{-1} = 4$ ps, $f = 0.01$, and $\epsilon_\infty = 2.8$, in reference to the dielectric properties of the C−H deformation vibration of 4,4′-bis(*N*-carbazolyl)-1,1′-biphenyl (CBP).[35] Note that the results presented are not in any way tied to a specific material and can be shown in general for other material parameters.

To first demonstrate the weak and strong coupling behavior of the system, we vary the thickness, s, of the vibrational mode layer. The graphene plasmon frequency is tuned to match the vibrational mode frequency via electrostatic gating. The absorption spectra for strong and weak coupling in Figure 1b,c show line shapes (solid lines) that are qualitatively different. In the strong coupling case, the absorption spectrum shows two distinct peaks that are well separated in frequency. The splitting in frequency is due to hybridization between the plasmon and the vibrational modes, resulting in a region of near-zero absorption with no excitations. For the weak coupling case, we see a sharp transparency window within a broader absorption peak. This behavior is analogous to the electromagnetically induced transparency (EIT),[2] produced by a destructive interference between the plasmon and the vibrational modes.[18,36] While the absorption spectrum for both strong and weak coupling has a transparency region at ω_0, the corresponding field patterns shown in Figure 1d are clearly dissimilar. The strong coupling case shows negligible field excitation when compared to the weak coupling case in which a strongly excited plasmon field is observed. This observation is consistent since the transparency in the weak coupling case arises not from an absence of modes but rather from an interaction between the modes resulting in destructive interference.

While the peaks of the absorption spectra are typically identified with the coupled mode frequencies, such an approach is only valid in the strongly coupled regime when the modes are clearly separated in frequency. When the system is in the weak coupling regime or near the transition between weak and strong coupling, the absorption peaks will not always correspond to the modes of the two isolated systems. Indeed, there has been considerable discussion on distinguishing between strong and weak light−matter coupling through its extinction/absorption spectrum.[3,4,37,38] A precise classification can be facilitated by using the harmonic inversion analysis method,[26] which spectrally decomposes the absorption spectrum into a superposition of complex Lorentzian resonances, with the form

$$A(\omega) = \mathrm{Im}\left(\sum_i \frac{d_i}{\omega - \omega_i - i\gamma_i}\right) \tag{10}$$

where d_i determines the line shape of the decomposed resonance, while ω_i and γ_i are the resonance frequency and scattering rates, respectively. Results of the harmonic inversion analysis applied to absorption spectra are shown as dashed lines in Figure 1b,c. In the weak coupling limit, the decomposed mode frequencies are degenerate with contrasting line widths, as in EIT. For the strong coupling limit, mode frequencies are well separated, indicating hybridized modes. Thus, the harmonic analysis clearly demonstrates that two different physical mechanisms are responsible for the two types of lineshapes.

https://doi.org/10.1021/acsphotonics.1c01083
ACS Photonics XXXX, XXX, XXX−XXX

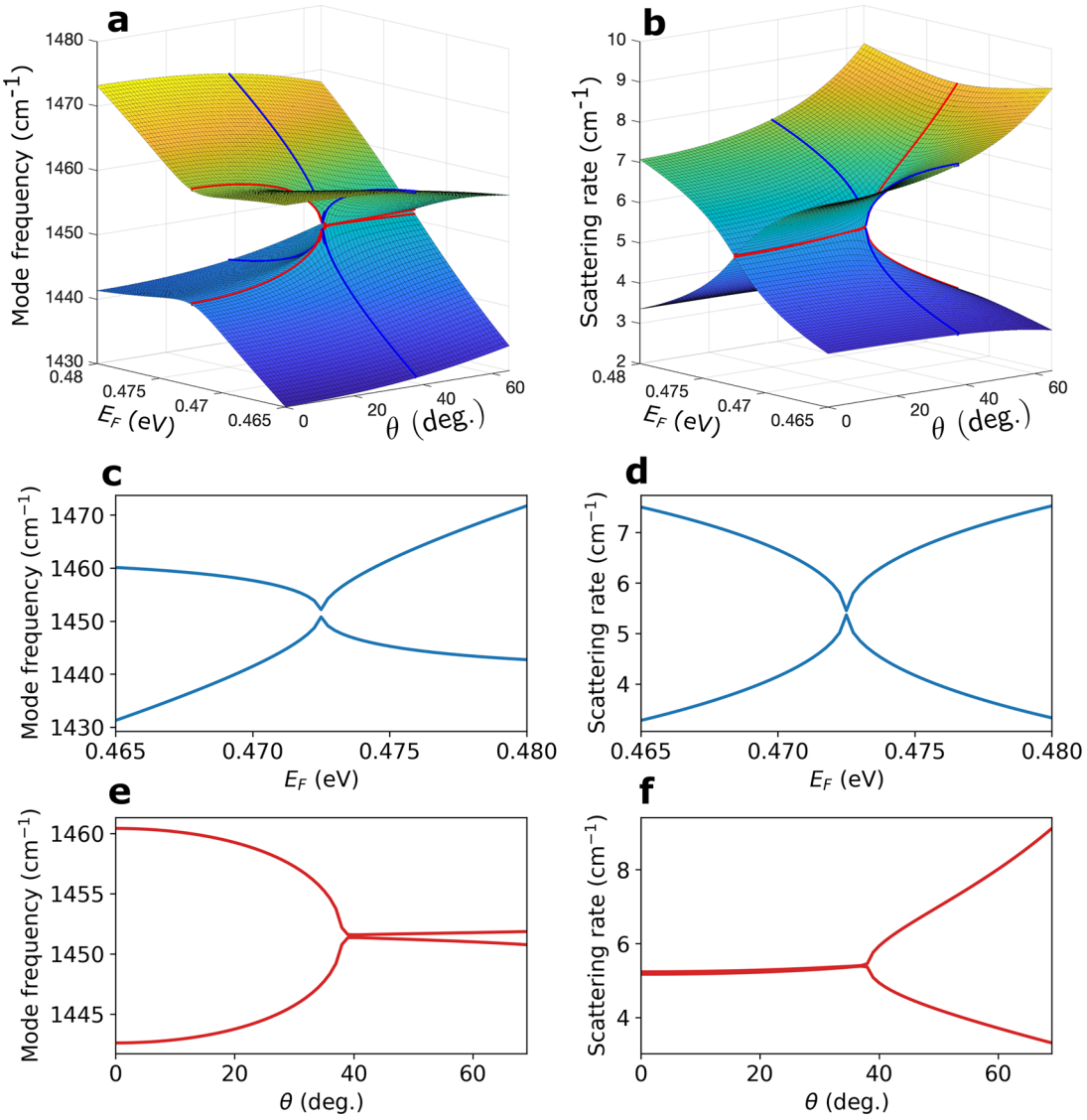

Figure 2. (a, b) Mode frequency and scattering rates extracted from the calculated absorption spectra as a function of E_F and θ are shown to be self-intersecting Riemann surfaces. (c, d) A slice of the Riemann surfaces at constant θ clearly show the simultaneous merging of the mode frequency and scattering rate. (e, f) Along constant E_F at which $\omega_{pl}(E_F) = \omega_0$, we see that a PT-breaking transition is observed as a function of θ.

Discussion on the efficacy of the harmonic inversion method to decompose the absorption spectrum is given in the Supporting Information (SI).

Having seen the strong and weak coupling regimes of the system, we now examine it more closely and show that an exceptional point exists at the transition point from weak to strong coupling. To find the exceptional point, we need at least two tunable parameters to probe the parameter space in which the exceptional point exists. From eq 4 we see that ω_{pl} and either κ or γ needs to be tuned. The ribbon width, along with the Fermi energy, will affect the plasmon frequency according to the relation $\omega_{pl}^2 = q|E_F|e^2/2\pi\hbar^2\epsilon_0$. The ribbon width defines the excited plasmon wavevector by $q = \pi/W$. In an experimental setting, the ribbon width will also have an effect on the damping of the plasmon originating from scattering off the ribbon edges.[16] Therefore, to minimize variations in the edge damping and take advantage of the electrical tunability of the system we use the Fermi energy to control the plasmon frequency. As a second tuning parameter, we show that the angle of incidence effectively tunes the loss of the system.

By comparing expressions derived from the coupled mode equations in eq 1 and from conventional electromagnetic scattering calculations (see SI), we find that the extrinsic loss of the plasmon is given by

$$\gamma_{pl,e} = \frac{\mu_0 cFD}{8\pi \cos\theta} \tag{11}$$

where $D = e^2E_F/\hbar^2$ is the Drude weight and $F = w/p$ is the filling factor. To physically understand the angle dependence, consider the plasmon to be an oscillating dipole oriented along the x-axis. $\gamma_{pl,e}$ describes the radiative loss of the plasmon through coupling to free space plane wave channels. The far-field radiation of the dipole is then independent of the angle θ (Figure 1a). Translational invariance along the y-direction implies that the free-space plane waves provide a uniform sampling of k_y. However, the plane wave channels do not uniformly sample θ; the number of states in an interval $\delta\theta$ is $\delta N = \delta\theta \cos\theta/\Delta k$, where Δk is the spacing of k-states.[39] Hence, for isotropic radiation, the out-coupling strength to a plane wave channel at angle θ must be $\gamma_{pl,e}(\theta) \propto (\cos\theta)^{-1}$.

https://doi.org/10.1021/acsphotonics.1c01083
ACS Photonics XXXX, XXX, XXX−XXX

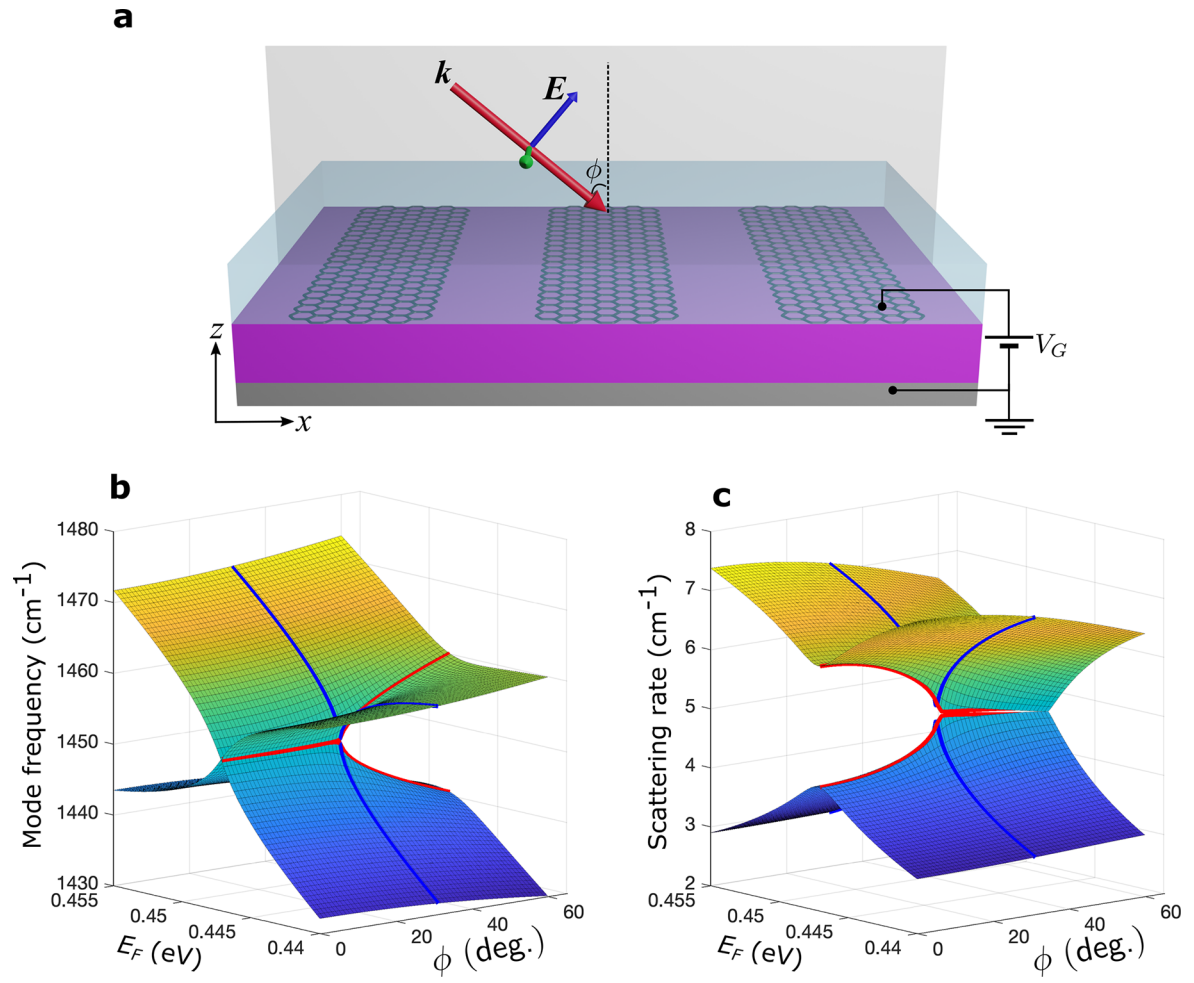

Figure 3. (a) Schematic of the modified configuration for incident light. (b, c) Mode frequency and scattering rate as a function of E_F and ϕ.

For s = 8 nm, we calculate the absorption for $E_F \in [0.465, 0.48]$ eV and $\theta \in [0,70]$ degrees, then apply the spectral decomposition using eq 10. The resulting mode frequencies and scattering rates are plotted as a surface in Figure 2a. We indeed observe the characteristic self-intersecting Riemann surface topology of an exceptional point.[8] Slices along E_F and θ further confirm the simultaneous crossing of the mode frequencies and scattering rates, showing the existence of an exceptional point. Figure 2e,f shows a PT-symmetry breaking transition along which the system evolves from strong to weak coupling. Thus, we can identify the exceptional point as the transition point between strong and weak coupling. For a given vibrational mode, the required Fermi energy may be lowered by using ribbons with a smaller width. In general, it is also possible to locate an exceptional point at lower Fermi energy if the graphene plasmon is coupled to a vibrational mode at lower frequency.

One limitation of the presented setup is that the system can only be tuned from strong to weak coupling as the angle of incidence θ is moved away from the normal. This indicates that locating the EP will not be possible when the vibrational mode of interest is weakly coupled to the graphene plasmon. Interestingly, we find that by simply rotating the plane of incidence by 90° and using p-polarized light (see Figure 3a), the system can be tuned from weak to strong coupling as we move away from normal incidence. In such a configuration, the far-field plasmon radiation is now proportional to $(\cos \phi)^2$. Since we still have $\delta N = \delta\phi \cos \phi/\Delta k$, it follows that $\gamma_{pl,e}(\phi) \propto \cos \phi$.

To observe the transition from weak to strong coupling as a function of ϕ, we now set s = 5.5 nm such that the plasmon and vibrational mode are weakly coupled at normal incidence. The mode frequencies and scattering rates are plotted in Figure 3b,c, and we once again observe the self-intersecting Riemann surface and the exceptional point. Compared to Figure 2a,b, note how the dependence on incident angle is now reversed, indicating that we are tuning the system in the opposite direction with the modified configuration.

DETECTION OF THE EP AND IMPLICATIONS FOR OPTICAL SENSING

We have shown that a typical plasmon-vibrational mode coupled system has an exceptional point that can be accessed via tuning of incident angle and Fermi energy. We now show that once the system is tuned to the exceptional point, sensitivity to perturbations in the thickness of the vibrational mode layer, which modify both the plasmon frequency and coupling strength, can be significantly enhanced. For simplicity, we will consider the case of normal incidence in this section. Then by electrostatically tuning the graphene Fermi energy to E_F = 0.4635 eV, we find the exceptional point when the layer thickness is $s = s^{EP}$ = 7.2 nm (see Figure 4a,b). Plotting the splitting in mode frequencies ($\Delta\omega$) and scattering rates ($\Delta\gamma$) as a function of perturbations to the film thickness (Δs), we show in Figure 4c that the expected square-root dependence of eigenvalue splitting on perturbations is indeed observed.

https://doi.org/10.1021/acsphotonics.1c01083
ACS Photonics XXXX, XXX, XXX−XXX

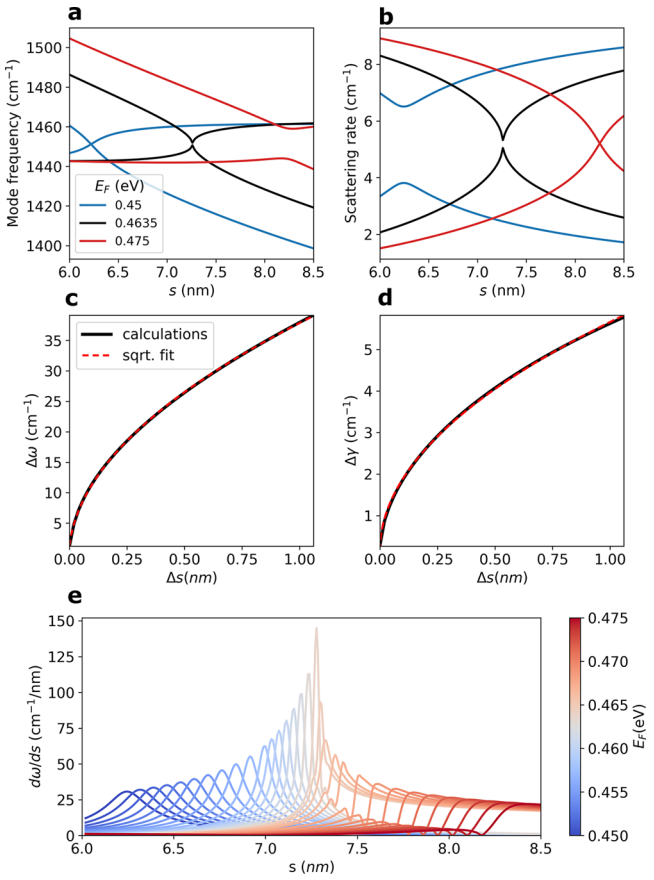

Figure 4. (a, b) Mode frequency and scattering rate as a function of thin film thickness. The simultaneous crossing of real and imaginary parts for $E_F = 0.4635$ eV reveals the exceptional point. (c, d) Mode frequency and scattering rate splitting as a function of $\Delta s = s - s^{EP}$, where s^{EP} is the thickness at which both the mode frequency and scattering rate are degenerate. Fermi energy is set to $E_F = E_F^{EP} = 0.4635$ eV. (d) Spectral sensitivity ($d\omega/ds$) as a function of film thickness for different values of E_F.

As an alternative measure for sensitivity of the spectrum of the system to small changes in the film thickness, we define $d\omega/ds$ as the thickness sensitivity. From the thickness sensitivity as a function of thickness for different values of E_F, shown in Figure 4d, we observe that sensitivity is indeed maximized when tuned to the exceptional point. Hence, for a localized region around the s^{EP}, the thickness sensitivity can be significantly enhanced. Furthermore, by changing the incident angle of light in either of the configurations mentioned, s^{EP} can be shifted to the thickness at which enhanced sensitivity is required. Thus, for applications in which we know the target thickness a priori, our configuration can be utilized to enhance sensitivity to minute changes in the thickness.

CONCLUSION

By applying a non-Hermitian framework to the plasmon-vibrational mode system and with the help of harmonic inversion analysis, we have shown that an exceptional point can be found at the boundary between weak and strong coupling. Such an interpretation can facilitate the classification of various coupling phenomena observed for coupled polariton modes. The observation of different coupling regimes typically requires the repeated fabrication of the sample to change either the physical distance between the coupled modes or the mode strength. By using two different configurations for varying the angle of incident light, along with the gate tunability of graphene, we show that the system can be tuned both from the strong to weak and weak to strong coupling regimes.

Furthermore, the existence of an exceptional point at the boundary between weak and strong coupling indicates that an enhanced sensing of vibrational modes can be achieved even in the intermediate coupling regime. Although the sensitivity of the exceptional point implies that small fabrication errors can perturb the system away from the exceptional point, tunablility of the proposed system via incident angle and Fermi energy allows us to reach the exceptional point to great proximity. Once the system is tuned close to the exceptional point, we demonstrate that minute perturbations to the molecular layer thickness are visible in the measured absorption spectrum.

METHODS

The absorption spectrum was obtained through a numerical calculation of the scattering coefficients. The calculation is set up by defining three dielectric regions with dielectric functions $\epsilon_j(\omega)$ and a surface conductivity $\sigma_j(\omega)$ at each boundary (see Figure 5).

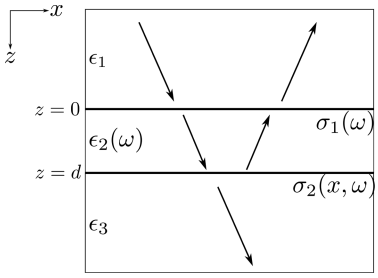

Figure 5. Schematic for the scattering coefficient calculation setup.

The surface conductivity of graphene nanoribbons is defined using a Fourier series expansion,

$$\sigma(x) = \sum_m \tilde{\sigma}_m e^{imGx}, \quad \tilde{\sigma}_m = \frac{1}{a}\int_0^a \sigma(x)e^{-imGx}\,dx \tag{12}$$

and is placed at the boundary $z = d$. The molecular layer is modeled as a bulk dielectric with a dielectric function given by the Lorentzian dipole model. For calculations presented in this work, $\sigma_1 = 0$.

s-Polarized Incidence. First consider the configuration shown in Figure 1a, which gives s-polarized incident light. The incident wave vector is $k^{inc} = (0, k_y, k_z)$ and the fields in each region are given by

$$\text{region } 1(z<0)\text{: } E_x^1 = E_x^{inc}e^{ik_y y}e^{ik_z z}\delta_{n,0} + \sum_n E_{x,n}^{1r}e^{ik_y y}e^{inGx}e^{-i\gamma_{1,n}z} \tag{13}$$

$$\text{region } 2(0<z<d)\text{: } E_x^2 = \sum_n [E_{x,n}^{2r}e^{-i\gamma_{2,n}z} + E_{x,n}^{2t}e^{i\gamma_{2,n}z}]e^{inGx}e^{ik_y y} \tag{14}$$

$$\text{region } 3(z>d)\text{: } E_x^3 = \sum_n E_{x,n}^{3t}e^{i\gamma_{3,n}z}e^{inGx}e^{ik_y y} \tag{15}$$

where $G = 2\pi/a$ and $\gamma_{j,n} = \sqrt{\frac{\epsilon_j\omega^2}{c^2} - (nG)^2 - k_y^2}$. The nth diffracted mode will have a wave vector $\mathbf{k}_{j,n} = (nG, k_y, \gamma_{j,n})$. For $n \neq 0$, since $G \gg k_y$, we may assume that $\mathbf{k}_{j,n} \approx (nG, 0, \gamma_{j,n})$. Applying boundary conditions at $z = 0$ and $z = d$, we find the relations

https://doi.org/10.1021/acsphotonics.1c01083
ACS Photonics XXXX, XXX, XXX−XXX

$$E_x^{\mathrm{inc}}\delta_{n,0} + E_{x,n}^{1r} = E_{x,n}^{2r} + E_{x,n}^{2t} \tag{16a}$$

$$\begin{cases} E_{x,0}^{2t}(\gamma_{1,0} + \gamma_{2,0}) + E_{x,0}^{2r}(\gamma_{1,0} - \gamma_{2,0}) = 2k_z E_x^{\mathrm{inc}}, & \text{for } n = 0 \\ E_{x,n}^{2t}\left(\dfrac{\epsilon_1}{\gamma_{1,n}} + \dfrac{\epsilon_2}{\gamma_{2,n}}\right) + E_{x,n}^{2r}\left(\dfrac{\epsilon_1}{\gamma_{1,n}} - \dfrac{\epsilon_2}{\gamma_{2,n}}\right) = 0, & \text{for } n \neq 0 \end{cases} \tag{16b}$$

$$E_{x,n}^{2r}e^{-i\gamma_{2,n}d} + E_{x,n}^{2t}e^{i\gamma_{2,n}d} = E_{x,n}^{3t}e^{i\gamma_{3,n}d} \tag{16c}$$

$$\begin{cases} E_{x,0}^{2t}(\gamma_{3,0} - \gamma_{2,0})e^{i\gamma_{2,n}d} + E_{x,0}^{2r}(\gamma_{3,0} + \gamma_{2,0})e^{-i\gamma_{2,n}d} + \mu_0\omega\displaystyle\sum_l \tilde{\sigma}_{-l}(E_{x,l}^{2t} + E_{x,l}^{2r}) \\ \quad = 0, \quad \text{for } n = 0 \\ E_{x,n}^{2t}\left(\dfrac{\epsilon_3}{\gamma_{3,n}} - \dfrac{\epsilon_2}{\gamma_{2,n}}\right)e^{i\gamma_{2,n}d} + E_{x,n}^{2r}\left(\dfrac{\epsilon_3}{\gamma_{3,n}} + \dfrac{\epsilon_2}{\gamma_{2,n}}\right)e^{-i\gamma_{2,n}d} \\ \quad + \dfrac{1}{\omega\epsilon_0}\displaystyle\sum_l \tilde{\sigma}_{n-l}(E_{x,l}^{2t} + E_{x,l}^{2r}) = 0, \quad \text{for } n \neq 0 \end{cases} \tag{16d}$$

If we consider modes in the range $n \in [-N,N]$, eq 16 can be cast into a $(4N + 2) \times (4N + 2)$ matrix equation that is numerically solved to give the fields in each region.

p-Polarized Incidence. For p-polarized incidence, the incident wave vector is $\mathbf{k}^{\mathrm{inc}} = (q, 0, k_z)$. The fields in each region are then

$$\text{region } 1(z < 0)\text{: } E_x^1 = E_x^{\mathrm{inc}}e^{iqx}e^{ik_z z} + \sum_n E_{x,n}^{1r}e^{i(q+nG)}e^{-i\gamma_{1,n}z} \tag{17}$$

$$\text{region } 2(0 < z < d)\text{: } E_x^2 = \sum_n [E_{x,n}^{2r}e^{-i\gamma_{2,n}z} + E_{x,n}^{2t}e^{i\gamma_{2,n}z}]e^{i(q+nG)x} \tag{18}$$

$$\text{region } 3(z > d)\text{: } E_x^3 = \sum_n E_{x,n}^{3t}e^{i\gamma_{3,n}z}e^{i(q+nG)x} \tag{19}$$

where $G = 2\pi/a$ is the reciprocal lattice vector and $\gamma_{j,n} = \sqrt{\frac{\epsilon_j\omega^2}{c^2} - (q + nG)^2}$ is the z-component wavevector of the nth mode in region j. Using Maxwell's equations and applying boundary conditions for the electric and magnetic fields at $z = 0$ and $z = d$ gives us

$$E_x^{\mathrm{inc}}\delta_{n,0} + E_{x,n}^{1r} = E_{x,n}^{2r} + E_{x,n}^{2t} \tag{20a}$$

$$E_{x,n}^{2t}\left(\frac{\epsilon_1}{\gamma_{1,n}} + \frac{\epsilon_2}{\gamma_{2,n}}\right) + E_{x,n}^{2r}\left(\frac{\epsilon_1}{\gamma_{1,n}} - \frac{\epsilon_2}{\gamma_{2,n}}\right) + \frac{1}{\epsilon_0\omega}\sum_l \tilde{\sigma}_{n-l}(E_{x,l}^{2t} + E_{x,l}^{2r}) = \frac{2\epsilon_1}{k_z}E_x^{\mathrm{inc}}\delta_{n,0} \tag{20b}$$

$$E_{x,n}^{2r}e^{-i\gamma_{2,n}d} + E_{x,n}^{2t}e^{i\gamma_{2,n}d} = E_{x,n}^{3t}e^{i\gamma_{3,n}d} \tag{20c}$$

$$E_{x,n}^{2t}\left(\frac{\epsilon_3}{\gamma_{3,n}} - \frac{\epsilon_2}{\gamma_{2,n}} + \frac{\sigma_{\mathrm{pol}}}{\epsilon_0\omega}\right)e^{i\gamma_{2,n}d} + E_{x,n}^{2r}\left(\frac{\epsilon_3}{\gamma_{3,n}} + \frac{\epsilon_2}{\gamma_{2,n}} + \frac{\sigma_{\mathrm{pol}}}{\epsilon_0\omega}\right)e^{-i\gamma_{2,n}d} = 0 \tag{20d}$$

If we consider modes in the range $n \in [-N,N]$, eq 20 can be cast into a $(4N + 2) \times (4N + 2)$ matrix equation that is numerically solved to give the fields in each region.

Field Maps. The field maps shown in Figure 1d were simulated using the electromagnetic waves, frequency domain module of COMSOL Multiphysics. Graphene was modeled as a surface current density with the conductivity given by eq 6. The molecular layer was modeled using the dielectric function in eq 9

■ ASSOCIATED CONTENT

Supporting Information

The Supporting Information is available free of charge at https://pubs.acs.org/doi/10.1021/acsphotonics.1c01083.

Simulated field maps for frequencies above and below the vibrational mode frequency in the strong coupling limit; Numerically calculated absorption spectra used to find eigenvalue surfaces in Figures 2 and 3; Anayltic expression for the angle-dependent loss; Efficacy analysis of the harmonic inversion method (PDF)

■ AUTHOR INFORMATION

Corresponding Authors

Sang Hyun Park − *Department of Electrical and Computer Engineering, University of Minnesota, Minneapolis, Minnesota 55455, United States*; Email: park2451@umn.edu

Shengxuan Xia − *Department of Electrical and Computer Engineering, University of Minnesota, Minneapolis, Minnesota 55455, United States; School of Physics and Electronics, Hunan University, Changsha 410082, China;* orcid.org/0000-0002-3158-6257; Email: shengxuanxia@hnu.edu.cn

Sang-Hyun Oh − *Department of Electrical and Computer Engineering, University of Minnesota, Minneapolis, Minnesota 55455, United States;* orcid.org/0000-0002-6992-5007; Email: sang@umn.edu

Phaedon Avouris − *Department of Electrical and Computer Engineering, University of Minnesota, Minneapolis, Minnesota 55455, United States; IBM Thomas J. Watson Research Center, Yorktown Heights, New York 10598, United States*; Email: avour001@umn.edu

Tony Low − *Department of Electrical and Computer Engineering, University of Minnesota, Minneapolis, Minnesota 55455, United States;* orcid.org/0000-0002-5759-5899; Email: tlow@umn.edu

Complete contact information is available at: https://pubs.acs.org/10.1021/acsphotonics.1c01083

Notes

The authors declare no competing financial interest.

■ ACKNOWLEDGMENTS

S.H.P. and T.L. acknowledge funding support from NSF/EFRI under Grant Agreement No. 1741660. S.-H.O. and T.L. acknowledge funding support from NSF ECCS No. 1809723. S.X. acknowledges funding support from the Natural Science Foundation of Hunan Province, China Grant No. 2020JJ5028.

■ REFERENCES

(1) Liu, X.; Galfsky, T.; Sun, Z.; Xia, F.; Lin, E. C.; Lee, Y. H.; Kéna-Cohen, S.; Menon, V. M. Strong light-matter coupling in two-dimensional atomic crystals. *Nat. Photonics* **2015**, *9*, 30−34.

(2) Fleischhauer, M.; Imamoglu, A.; Marangos, J. P. Electromagnetically induced transparency: Optics in coherent media. *Rev. Mod. Phys.* **2005**, *77*, 633−673.

(3) Anisimov, P. M.; Dowling, J. P.; Sanders, B. C. Objectively discerning Autler-Townes splitting from electromagnetically induced transparency. *Phys. Rev. Lett.* **2011**, *107*, 163604.

(4) Peng, B.; Özdemir, S. K.; Chen, W.; Nori, F.; Yang, L. What is and what is not electromagnetically induced transparency in whispering-gallery microcavities. *Nat. Commun.* **2014**, *5*, 5082.

(5) Garrido Alzar, C. L.; Martinez, M. A. G.; Nussenzveig, P. Classical analog of electromagnetically induced transparency. *Am. J. Phys.* **2002**, *70*, 37−41.

(6) Zhang, S.; Genov, D. A.; Wang, Y.; Liu, M.; Zhang, X. Plasmon-induced transparency in metamaterials. *Phys. Rev. Lett.* **2008**, *101*, 047401.
(7) Törmä, P.; Barnes, W. L. Strong coupling between surface plasmon polaritons and emitters: a review. *Rep. Prog. Phys.* **2015**, *78*, 013901.
(8) El-Ganainy, R.; Makris, K. G.; Khajavikhan, M.; Musslimani, Z. H.; Rotter, S.; Christodoulides, D. N. Non-Hermitian physics and PT symmetry. *Nat. Phys.* **2018**, *14*, 11−19.
(9) Guo, A.; Salamo, G. J.; Duchesne, D.; Morandotti, R.; Volatier-Ravat, M.; Aimez, V.; Siviloglou, G. A.; Christodoulides, D. N. Observation of P T -Symmetry Breaking in Complex Optical Potentials. *Phys. Rev. Lett.* **2009**, *103*, 093902.
(10) Rüter, C. E.; Makris, K. G.; El-Ganainy, R.; Christodoulides, D. N.; Segev, M.; Kip, D. Observation of parity-time symmetry in optics. *Nat. Phys.* **2010**, *6*, 192−195.
(11) Lawrence, M.; Xu, N.; Zhang, X.; Cong, L.; Han, J.; Zhang, W.; Zhang, S. Manifestation of PT symmetry breaking in polarization space with terahertz metasurfaces. *Phys. Rev. Lett.* **2014**, *113*, 093901.
(12) Hodaei, H.; Miri, M.-a.; Heinrich, M.; Christodoulides, D. N.; Khajavikhan, M. Parity-time-symmetric microring lasers. *Science (Washington, DC, U. S.)* **2014**, *346*, 975−978.
(13) Wiersig, J. Review of exceptional point-based sensors. *Photonics Res.* **2020**, *8*, 1457.
(14) Hodaei, H.; Hassan, A. U.; Wittek, S.; Garcia-Gracia, H.; El-Ganainy, R.; Christodoulides, D. N.; Khajavikhan, M. Enhanced sensitivity at higher-order exceptional points. *Nature* **2017**, *548*, 187−191.
(15) Chen, W.; Özdemir, S. K.; Zhao, G.; Wiersig, J.; Yang, L. Exceptional points enhance sensing in an optical microcavity. *Nature* **2017**, *548*, 192−196.
(16) Yan, H.; Low, T.; Zhu, W.; Wu, Y.; Freitag, M.; Li, X.; Guinea, F.; Avouris, P.; Xia, F. Damping pathways of mid-infrared plasmons in graphene nanostructures. *Nat. Photonics* **2013**, *7*, 394−399.
(17) Brar, V. W.; Jang, M. S.; Sherrott, M.; Kim, S.; Lopez, J. J.; Kim, L. B.; Choi, M.; Atwater, H. Hybrid Surface-Phonon-Plasmon Polariton Modes in Graphene/Monolayer h-BN Heterostructures. *Nano Lett.* **2014**, *14*, 3876−3880.
(18) Yan, H.; Low, T.; Guinea, F.; Xia, F.; Avouris, P. Tunable phonon-induced transparency in bilayer graphene nanoribbons. *Nano Lett.* **2014**, *14*, 4581−4586.
(19) Bezares, F. J.; et al. Intrinsic Plasmon-Phonon Interactions in Highly Doped Graphene: A Near-Field Imaging Study. *Nano Lett.* **2017**, *17*, 5908−5913.
(20) Rodrigo, D.; Limaj, O.; Janner, D.; Etezadi, D.; García de Abajo, F. J.; Pruneri, V.; Altug, H. Mid-infrared plasmonic biosensing with graphene. *Science (Washington, DC, U. S.)* **2015**, *349*, 165−168.
(21) Farmer, D. B.; Avouris, P.; Li, Y.; Heinz, T. F.; Han, S. J. Ultrasensitive Plasmonic Detection of Molecules with Graphene. *ACS Photonics* **2016**, *3*, 553−557.
(22) Hu, H.; Yang, X.; Guo, X.; Khaliji, K.; Biswas, S. R.; García de Abajo, F. J.; Low, T.; Sun, Z.; Dai, Q. Gas identification with graphene plasmons. *Nat. Commun.* **2019**, *10*, 1131.
(23) Khaliji, K.; Biswas, S. R.; Hu, H.; Yang, X.; Dai, Q.; Oh, S.-H.; Avouris, P.; Low, T. Plasmonic Gas Sensing with Graphene Nanoribbons. *Phys. Rev. Appl.* **2020**, *13*, 011002.
(24) Lee, I.-H.; Yoo, D.; Avouris, P.; Low, T.; Oh, S.-H. Graphene acoustic plasmon resonator for ultrasensitive infrared spectroscopy. *Nat. Nanotechnol.* **2019**, *14*, 313−319.
(25) Oh, S.-H.; Altug, H.; Jin, X.; Low, T.; Koester, S. J.; Ivanov, A. P.; Edel, J. B.; Avouris, P.; Strano, M. S. Nanophotonic biosensors harnessing van der Waals materials. *Nat. Commun.* **2021**, *12*, 3824.
(26) Fuchs, J.; Main, J.; Cartarius, H.; Wunner, G. Harmonic inversion analysis of exceptional points in resonance spectra. *J. Phys. A: Math. Theor.* **2014**, *47*, 125304.
(27) Haus, H. *Waves and Fields in Optoelectronics*; Prentice-Hall, 1985.
(28) Bender, C. M.; Boettcher, S. Real spectra in non-hermitian hamiltonians having PT symmetry. *Phys. Rev. Lett.* **1998**, *80*, 5243−5246.
(29) Özdemir, K.; Rotter, S.; Nori, F.; Yang, L. Parity time symmetry and exceptional points in photonics. *Nat. Mater.* **2019**, *18*, 783−798.
(30) Nikitin, A. Y.; Low, T.; Martin-Moreno, L. Anomalous reflection phase of graphene plasmons and its influence on resonators. *Phys. Rev. B: Condens. Matter Mater. Phys.* **2014**, *90*, 041407.
(31) Goncalves, P.; Peres, N. M. *An Introduction to Graphene Plasmonics*; World Scientific, 2016.
(32) Principi, A.; Vignale, G.; Carrega, M.; Polini, M. Intrinsic lifetime of Dirac plasmons in graphene. *Phys. Rev. B: Condens. Matter Mater. Phys.* **2013**, *88*, 195405.
(33) Principi, A.; Vignale, G.; Carrega, M.; Polini, M. Impact of disorder on Dirac plasmon losses. *Phys. Rev. B: Condens. Matter Mater. Phys.* **2013**, *88*, 1214056.
(34) Novko, D. Dopant-Induced Plasmon Decay in Graphene. *Nano Lett.* **2017**, *17*, 6991−6996.
(35) Autore, M.; Li, P.; Dolado, I.; Alfaro-Mozaz, F. J.; Esteban, R.; Atxabal, A.; Casanova, F.; Hueso, L. E.; Alonso-González, P.; Aizpurua, J.; Nikitin, A. Y.; Vélez, S.; Hillenbrand, R. Boron nitride nanoresonators for Phonon-Enhanced molecular vibrational spectroscopy at the strong coupling limit. *Light: Sci. Appl.* **2018**, *7*, 17172−17178.
(36) Low, T.; Guinea, F.; Yan, H.; Xia, F.; Avouris, P. Novel midinfrared plasmonic properties of bilayer graphene. *Phys. Rev. Lett.* **2014**, *112*, 116801.
(37) Hao, L.; Jiao, Y.; Xue, Y.; Han, X.; Bai, S.; Zhao, J.; Raithel, G. Transition from electromagnetically induced transparency to Autler,-ÄíTownes splitting in cold cesium atoms. *New J. Phys.* **2018**, *20*, 073024.
(38) He, L.-Y.; Wang, T.-J.; Gao, Y.-P.; Cao, C.; Wang, C. Discerning electromagnetically induced transparency from Autler-Townes splitting in plasmonic waveguide and coupled resonators system. *Opt. Express* **2015**, *23*, 23817.
(39) Verslegers, L.; Yu, Z.; Catrysse, P. B.; Fan, S. Temporal coupled-mode theory for resonant apertures. *J. Opt. Soc. Am. B* **2010**, *27*, 1947.

https://doi.org/10.1021/acsphotonics.1c01083
ACS Photonics XXXX, XXX, XXX−XXX